



Final Draft
of the original manuscript:

Victoria-Hernandez, J.; Yi, S.; Klaumuenzer, D.; Letzig, D.:
Recrystallization behavior and its relationship with deformation mechanisms of a hot rolled Mg-Zn-Ca-Zr alloy.
In: Materials Science and Engineering A. Vol. 761 (2019) 138054.
First published online by Elsevier: 20.06.2019

<https://dx.doi.org/10.1016/j.msea.2019.138054>

Recrystallization behavior and its relationship with deformation mechanisms of a hot rolled Mg-Zn-Ca-Zr alloy

J. Victoria-Hernández^{1*}, S. Yi¹, D. Klaumünzer², D. Letzig¹

¹ Magnesium Innovation Centre, Helmholtz-Zentrum Geesthacht, Max-Planck-Str. 1,
Geesthacht D-21502, Germany

² Volkswagen AG, Group Research, Materials and Manufacturing Processes, Berliner Ring 2,
Wolfsburg D-38440, Germany

*corresponding author: jose.victoria-hernandez@hzg.de, j-victoria-hernandez@outlook.de

(J. Victoria-Hernández)

Telephone: +494152871919, Fax: +494152871927

Abstract

The microstructure-texture evolution of twin-roll-cast strips of an Mg-Zn-Ca-Zr alloy subjected to hot rolling and recrystallization annealing was investigated. Upon annealing, a distinctive change in the main texture components is observed from basal poles tilted towards the rolling direction (RD) to basal poles tilted towards the transverse direction (TD). X-ray diffraction analysis and EBSD measurements indicated that the distinct change of the texture components during recrystallization annealing is related to the weakening of the global texture intensity. It is demonstrated that the controlling mechanism of the microstructure development during the annealing is the growth of recovered volumes within deformed

grains in a regime of a continuous type of recrystallization. Recrystallized grains developed from the $\{1\ 0\ -1\ 1\}$ - $\{1\ 0\ -1\ 2\}$ secondary twinned areas were observed, which show a restricted contribution to the recrystallized microstructure formed in a discontinuous type of recrystallization. In-grain misorientation axis analysis from the as-rolled microstructure indicates that prismatic $\langle a \rangle$ together with basal $\langle a \rangle$ slip become the dominant dislocation modes for the grains with their c -axis inclined relative to the normal direction. Several grains with the orientations of the basal pole split to the transverse direction are the $\{1\ 0\ -1\ 2\}$ extension twins. This leads to a mirror symmetry of the basal poles along the transverse direction. It is observed that during recrystallization annealing, deformed volumes of grains containing $\{1\ 0\ -1\ 2\}$ extension twins can recover effectively. This leads to the development of grains having the TD-split orientation in the regime of continuous static recrystallization also known as extended recovery.

Keywords: Crystallographic texture; deformation mechanisms; recovery; continuous static recrystallization; discontinuous static recrystallization

1. Introduction

For the last two decades, wrought magnesium alloys have been in constant development to improve their formability, corrosion resistance, and recyclability. Progressive alloy development and the use of selected elements has led to significant improvements on ductility, mechanical properties and formability of wrought Mg alloys [1-3]. Rare-earth (RE) elements are among the most effective alloying elements for improving the formability of Mg. They can modify important aspects of the microstructure. They include alterations in the stacking fault energy leading to changes in the balance of dominant deformation modes

during deformation [4, 5], distinctive crystallographic textures that modify the balance of active deformation modes leading to improvements of formability [6-8] and, precipitation which can significantly strengthen the alloys [9, 10]. Crystallographic textures of rolled Mg-Zn-RE alloys are weak and tend to develop a broad scatter of basal planes with two peaks splitting towards the TD in the (0 0 0 1) pole figure [7, 11]. Such textures are linked to the improvement of formability at low temperatures [3, 8, 12]. Nevertheless, in recent years, a focus has been placed on RE free Mg alloys. In this direction, Ca is an effective element that can modify the microstructure and crystallographic texture [13, 14]. Mg-Zn-Ca alloys show similarities with respect to Mg-Zn-RE in terms of crystallographic textures, mechanical properties and forming behavior [13]. As shown in Refs. [1, 13], a similar room temperature stretch formability of Mg-Zn-Ce and Mg-Zn-Ca was obtained in comparison to 6000 series Al alloys. So far, there are numerous studies dealing with the mechanisms of texture development upon annealing of Mg-Zn-RE and Mg-Zn-Ca alloys [11, 15-17]. However, the controlling mechanisms on how the characteristic TD-split texture evolves from the deformed state to a recrystallized condition are not fully understood and continues to be a matter of debate. Mechanisms such as PSN have been discussed to control the texture development in Mg-RE alloys [18]. However, the characteristic texture modification effect of RE also occurs in solid solution alloys, hence, discarding PSN as the controlling mechanism for texture development [19, 20]. The nucleation of randomly recrystallized grains within shear bands has also been discussed to be very important for the weakening and eventual development of the characteristic texture of Mg-RE alloys [15, 16]. Nevertheless, as pointed out in ref. [17], conventional alloys such as AZ31 and Mg-Zn binary alloys also show extensive shear banding with related recrystallization during annealing. Those alloys, however, develop strong basal textures making the exact role of shear band nucleation unclear. Recently, there is more

evidence than Zn, RE and Ca tend to migrate and sit along the grain or twin boundaries, thus modifying the preferential growth of certain orientations during recrystallization annealing opening the possibilities of designing more ductile Mg alloys [17, 21, 22]. In this regard, during static recrystallization of cold rolled WE43 alloy, the nucleation and related growth of grains with specific orientations developing on $\{1\ 0\ -1\ 1\}$ - $\{1\ 0\ -1\ 2\}$ double twin boundaries was claimed to be the origin of the TD-split texture development [11]. However, in that study, two important aspects have to be taken into account. The cold rolling pass was performed on an extruded bar. Although, prior rolling the bar was previously homogenized, it had already a broad distribution of basal poles towards TD. Furthermore, it was claimed that the TD component mainly arises from the growth of recrystallized grains within $\{1\ 0\ -1\ 1\}$ - $\{1\ 0\ -1\ 2\}$ double twins. While many new recrystallized grains (with the respective TD-split orientation) developed from twinned volumes during annealing treatment, the TD-split texture was already visible in the deformation texture. Therefore, there must be other factors, which can lead to the development of the TD texture components. In this regard, the present study aims to clarify the link between the deformation mechanisms involved during rolling and their effect during primary recrystallization.

2. Experimental procedure

Mg-0.6Zn-0.6Ca-0.1Zr (wt. %) alloy strip with 5.2 mm thickness produced by twin-roll casting (TRC) was used for hot rolling experiments. A Novelis™ Jumbo 3CM twin-roll caster at Helmholtz-Zentrum Geesthacht was used for the production of the strip. Before rolling, the strip was homogenized at 450 °C for 16 h. Hot rolling was performed at 370 °C. It consisted of two initial rolling passes with $\varphi = 0.1$ and seven passes with $\varphi = 0.2$:

$$\varphi = -\ln\left(\frac{h_{n+1}}{h_n}\right) \quad (1)$$

where φ is true strain, n the number of the pass, and h_n the sample thickness after the n^{th} pass. After each rolling step, the sheet was reheated to the rolling temperature and held there for 10 min. After the last rolling pass, the samples were air-cooled.

Recrystallization annealing was performed at the rolling temperature for various times, 30, 90, 180 and 1800 s in order to capture the microstructure-texture development. Additionally, an extra annealing treatment at 450 °C for 1800 s was performed on an already recrystallized sample, i.e. at 370 °C for 1800 s, to promote grain growth and track the microstructure-texture change. For the annealing of samples used for optical microscopy, texture analysis and mechanical testing no inert atmosphere was employed. After reaching the annealing time, the samples were immediately water quenched to room temperature in order to preserve the microstructure and texture.

The metallographic examination was conducted by optical microscopy and electron backscatter diffraction (EBSD) on the normal direction (ND) and RD plane. Samples were ground with emery paper to grit 2500, and polished with a water-free suspension of silicon oxide (OPS 0.5 μm). Energy-dispersive X-ray spectroscopy (EDS) was performed on the mechanically polished samples to reveal the type and chemical composition of the secondary phase particles in the sheet.

EBSD measurements were carried out using a field emission gun scanning electron microscope Zeiss™ Ultra 55 equipped with an EDAX-TSL OIM™ system. The sample used for *ex-situ* measurements was electropolished using a Struers™ AC2 solution at 16 V for 35 s at -25 °C to obtain a surface free of defects, such as deformation from mechanical polishing and scratches. Measurements were also carried out on the ND-RD plane. EBSD measurements

were conducted with an acceleration voltage of 15 kV and a step size of 0.3 μm . To track the microstructure evolution at the early annealing stage, *ex-situ* EBSD measurements were carried out. After the EBSD measurement in the as-rolled condition, the sample was annealed in a conventional convection furnace filled with Argon to reduce surface oxidation, by which the EBSD measurements could be repeatedly conducted at the defined area after various annealing times. To slow down the recrystallization process, the temperature for the *ex-situ* EBSD measurement was set to 350 °C. Due to slow recrystallization kinetics resulting from the lower temperature and surface effect, as described in [17, 23], the annealing times were extended to 270, 570 and 1800 s to trigger the visible microstructural changes at the sample surface. It is to note, that the microstructure evolution during the *ex-situ* measurements shows no visible difference, in terms of the secondary phase particles and grain morphologies, in comparison to those from the bulk samples annealed at 370 °C.

Global texture was measured using a Panalytical™ X-ray diffractometer with Cu-K α radiation. The orientation distribution function (ODF) was calculated using the MTEX toolbox [24] from six measured pole figures (0 0 0 1), {1 0 -1 0}, {1 0 -1 1}, {1 0 -1 2}, {1 0 -1 3} and {1 1 -2 0}. The results are presented in terms of the recalculated (0 0 0 1), {1 0 -1 0} pole figures and ODF maps.

To verify the change in the mechanical response after annealing, tensile samples of 12.5 mm in width and 50 mm in gauge length (DIN-50125-H) were prepared from as-rolled and samples annealed at 370 °C for 30, 90 and 1800 s. Tensile tests were carried out in a Zwick 050™ universal testing machine. Three different sheet directions, i.e. RD, 45° to the RD, and TD, were tested. Tensile tests were performed at 10^{-3} s^{-1} of constant strain rate to the fracture. This was ensured by employing a clip-on extensometer that allowed the continuous

calibration of the strain rate during the experiment. The Lankford parameter (r_{10} -value) was evaluated at 10 % of uniform elongation.

3. Results

3.1 Microstructure development

Fig. 1a shows the microstructure in the mid-plane of the as-TRC strip. The microstructure consists of elongated deformed grains in the RD surrounded by small-recrystallized grains. It is important to highlight the good homogeneity in the microstructure, i.e. fine grain structure and the lack of center-line segregation. This is a result of using Zr as a grain refiner and working with a dilute alloy system as described in ref. [25]. In the as-cast strip, secondary phase particles are mostly found at the grain boundaries. The EDS analysis revealed that the particles are mainly Mg_2Ca laves phase. Only a few particles of the ternary $Mg_6Zn_3Ca_2$ phase were observed. Fig. 1b displays the microstructure of the strip after homogenization treatment. The microstructure is homogeneous with equiaxed grains. It is seen less Mg_2Ca particles along grain boundaries. The average grain size calculated with the linear intercept method is $17 \pm 9.2 \mu m$.

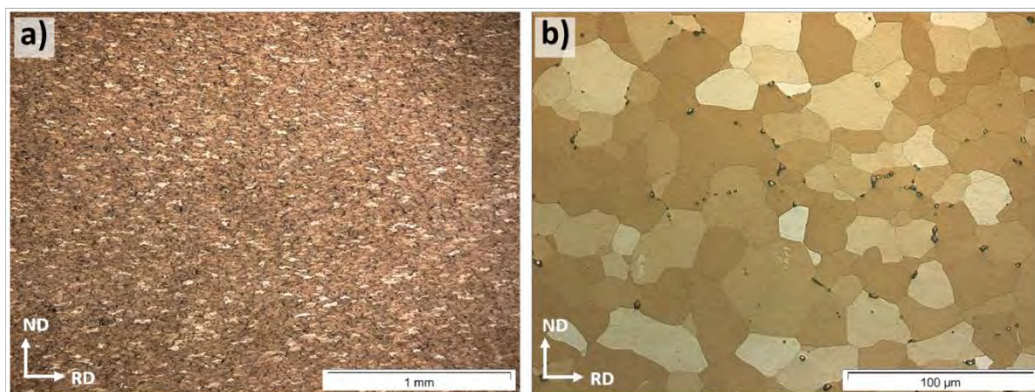


Fig. 1 Microstructures of the a) as-TRC strip and b) after homogenization annealing at 450° for 16 h.

The microstructure after hot rolling is presented in Fig. 2. In the as-rolled condition, deformed grains containing twins are revealed. Coarse Mg_2Ca phase particles are still located along grain boundaries. Some of them are fragmented and elongated towards RD, developing stringer-like structures. Additionally, many small and homogeneously distributed Mg_2Ca particles precipitate during the rolling and intermediate annealing process. The microstructure of the annealed sheet, Fig. 2b, shows a twin free and homogeneous grain structure. Many small particles formed along former twin boundaries are observed in Fig. 2b (see the inset). The segregation of Zn and Ca atoms in Mg-Zn-Ca alloys, and Zn and RE atoms in Mg-Zn-RE alloys to grain and twin boundaries, and subsequent precipitation behavior of secondary phase particles has also been previously observed in [11, 17]. The average grain size in the as-rolled condition is $6.3\pm 3.5\ \mu m$ (excluding twin boundaries). After annealing, the grain size slightly increases to $6.9\pm 3.2\ \mu m$.

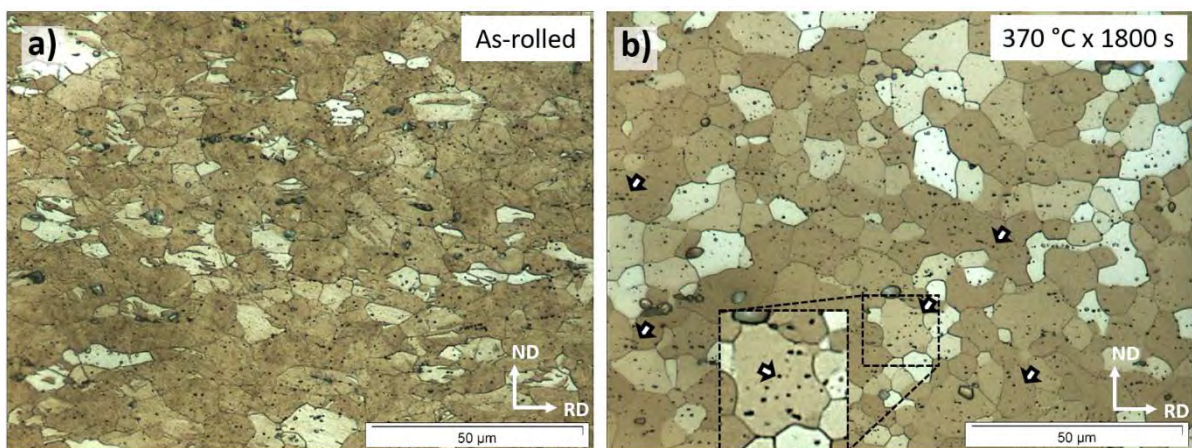


Fig. 2 Optical microstructures in a) as-rolled condition and b) after annealing at 370 °C for 1800 s.

In order to capture more details of the microstructure development, short annealing experiments were performed for different times. Fig. 3a shows the microstructure after annealing at 370 °C for 30 s. In comparison to the as-rolled condition, it shows neither an obvious change in the grain structure nor in the grain size which remains at $6.9\pm 3.5\ \mu\text{m}$. The microstructure after 90 s of annealing shows a partially recrystallized microstructure. There are still twin boundaries within a few grains and some grains do not have an equiaxed grain structure, as indicated by the arrows in Fig. 3b. The average grain size is $6.5\pm 3.9\ \mu\text{m}$. After 180 s of annealing, the recrystallization process seems to be completed. The microstructure has an equiaxed grain structure, no traces of deformation twins and a similar grain size of $6.4\pm 4.1\ \mu\text{m}$ is found (Fig. 3c). Grain growth was stimulated in a sample previously annealed at 370 °C for 1800 s by a subsequent annealing at 450 °C for 1800 s. The average grain size of the two-step annealed sample is $11.5\pm 6.9\ \mu\text{m}$. As an important feature, most of the small Mg_2Ca intragranular particles dissolved during annealing (see Fig. 3d).

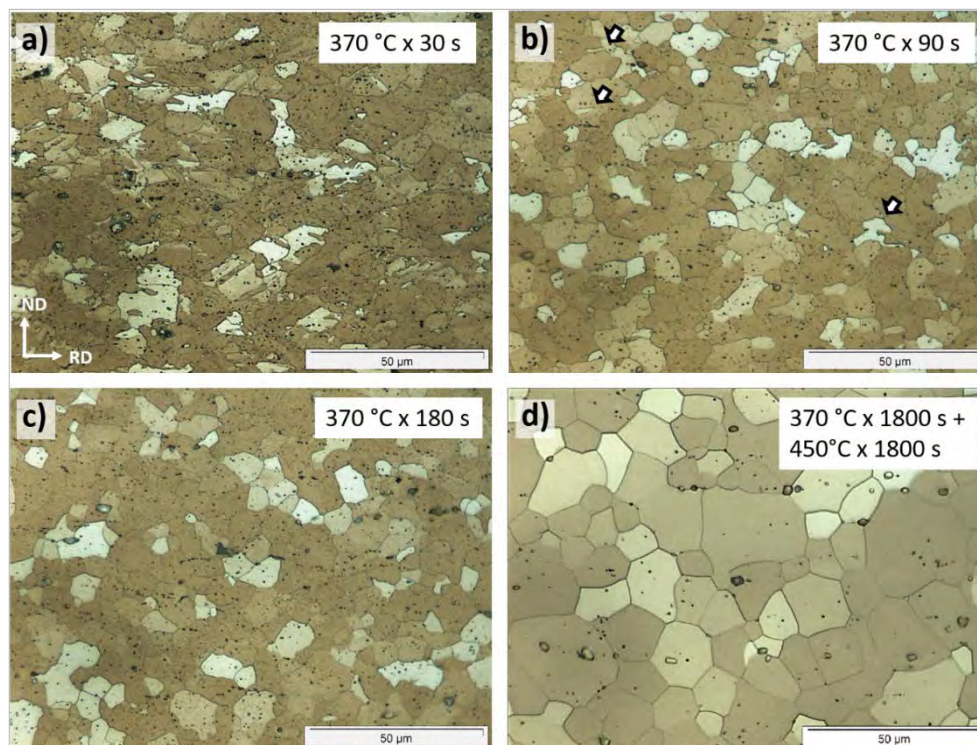


Fig. 3 Microstructural development after annealing at 370 °C for a) 30 s, b) 90 s, c) 180 s and d) sample recrystallized at 370 °C for 1800 s and subsequently annealed at 450 °C for 1800 s.

3.2 Texture development

Fig. 4a depicts the texture of the cast TRC strip. It shows a relatively strong texture intensity of 5.3 multiples of random distribution (m.r.d.). Two main peaks splitting from ND towards RD and the $\langle 1\ 0\ -1\ 0 \rangle$ pole parallel to RD are observed. A broad scatter of basal poles towards TD is also evident. After homogenization annealing, the texture is significantly weaker in comparison to the as-TRC one. The main texture components remain, yet they are slightly more inclined towards RD.

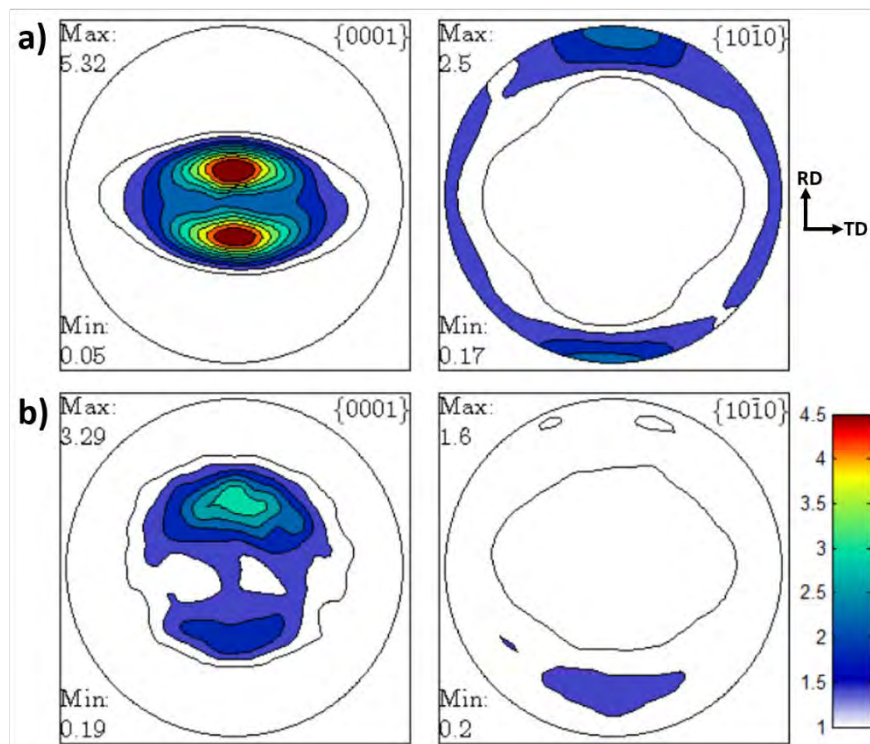


Fig. 4 XRD textures represented in terms of $(0\ 0\ 0\ 1)$ and $(1\ 0\ -1\ 0)$ pole figures for the a) as TRC strip and b) after homogenization annealing at 450 °C for 16 h.

Fig. 5 displays the texture development from the as-rolled to the annealed condition. The texture of the as-rolled sheet, Fig. 5a, shows many similarities with the as-TRC condition, i.e. basal poles split towards RD, a basal pole spread towards TD and the $\langle 1\ 0\ -1\ 0 \rangle$ parallel to RD. Annealing the material at 370 °C for 1800 s leads to a weak texture with the transition from an RD-split of the basal pole to a TD-split. The basal poles are mainly tilted by $\sim 35^\circ$ towards the TD. The texture component of $\langle 1\ 0\ -1\ 0 \rangle$ parallel to the RD is retained during the annealing (Fig. 5b). This texture development is rather similar to the recrystallization texture reported in Mg-Zn-RE alloys where a TD-split texture develops during annealing [1, 3, 7].

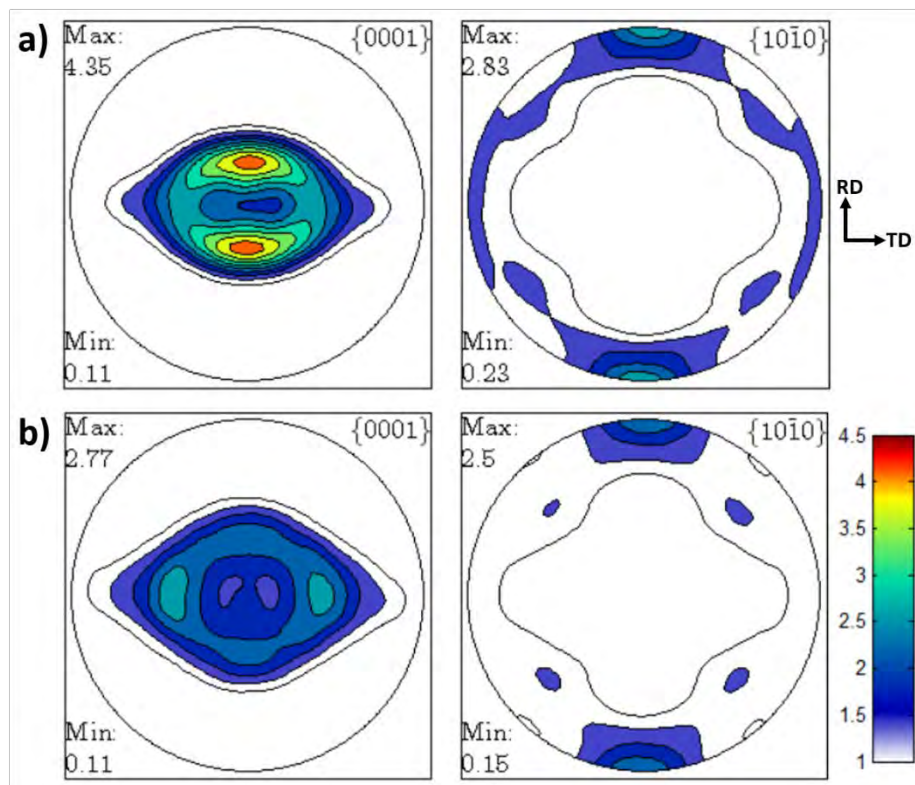


Fig. 5 XRD textures represented in terms of $(0\ 0\ 0\ 1)$ and $(1\ 0\ -1\ 0)$ pole figures for the a) as-rolled ZKK sheet and b) after recrystallization annealing at 370 °C for 1800 s.

Fig. 6 plots the texture evolution in terms of the $(0\ 0\ 0\ 1)$ pole figures as a function of the annealing time. To enhance clarity, the as-rolled texture is included in Fig. 6a. It shows the

symmetric split of the maximum pole intensities towards the RD at an angle of $\pm 10^\circ$ and towards the TD at an angle of $\pm 30^\circ$. Despite the negligible changes in the grain structure after 30 s of annealing time at 370 °C, the intensity of the main peaks tilted towards RD start to weaken as shown in Fig. 6b. After annealing for 90 s, the intensity of both RD-peaks weaken significantly and the two TD-peaks become visible (see the inset in Fig. 6c). It is to note that the intensity of the TD-peaks also weakens. However, the weakening degree is almost negligible, from 3.0 m.r.d. in the as-rolled state to 2.6 m.r.d. after 90 s annealing. This holds for extended annealing times of 180 and 1800 s (Figs. 6 d-e). Therefore, it is clear that the appearance of the TD-split peaks of the basal pole is related to the weakening of the overall texture intensities rather than a distinctive development of grains with the corresponding orientations. It is to highlight that such TD-orientations are rather stable and persist after recrystallization annealing. Moreover, a careful examination of the intensity profiles indicates that there is an increase of the intensities in the range of 65° - 90° along TD for the annealed samples. Despite the significant growth of grains in the sample annealed for a further 1800 s at 450 °C annealing, a slight change in the global texture is observed. The present results show that the grains with orientations close to 15 - 30° from ND to RD are the ones to be consumed during the grain growth stage (see Fig. 6f). As reported in [17], atomic segregation of Zn and Ca elements could influence the growth of specific types of grains. However, this aspect of grain growth after primary recrystallization is not discussed further in this study due to the slight texture modification.

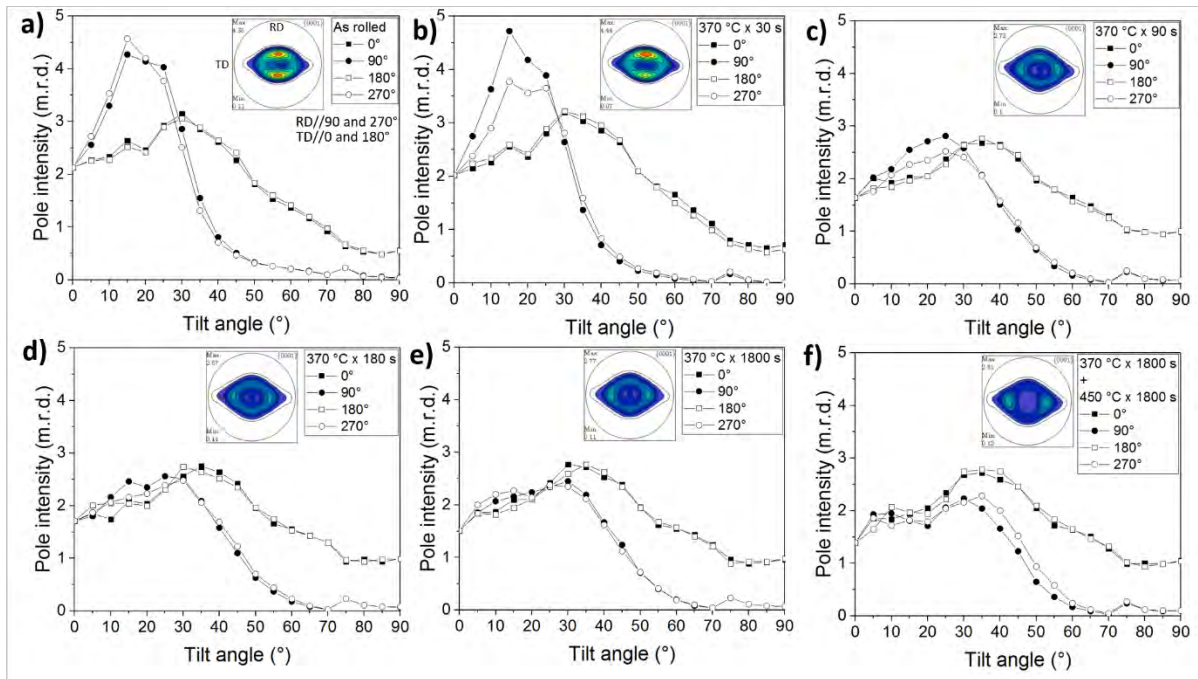


Fig. 6 Texture evolution in terms of the (0 0 0 1) pole figure for different annealing conditions. The intensity profiles are plotted as a function of the tilt from normal direction towards RD (90 and 270°) and TD (0-180°) for a) as-rolled state, b-e) annealed at 370 °C for 30, 90, 180, 1800 s respectively, and f) sample annealed at 370 °C for 1800 s plus an additional annealing at 450 °C for 1800 s.

To reveal the change of texture fibers and components during annealing two sections of the ODF and respective ODF intensity plots of the main fibers are presented in Figure 7. This representation has been used to clearly show the evolution of the texture fibers and components as a result of processing parameters of Zr-Nb composites [26], and to show the relationship of between deformation-recrystallization textures of Zr-2Hf alloy [27]. Exemplarily, the ODF sections ($\varphi_2=0^\circ$ and $\varphi_2=30^\circ$) from the as-rolled sample and from the sample annealed at 370 °C for 1800 s are presented in Fig. 7a and 7b, respectively. The complete set of ODF sections ($\varphi_2=0^\circ$ and $\varphi_2=30^\circ$) for the intermediate annealed samples is presented in the supplementary Fig. S1. In the $\varphi_2=30^\circ$ section of the as-rolled sample, it is

observed the presence of two relatively weak fibers, i.e. $\langle 1\ 0\ -1\ 0 \rangle$ fiber ($\phi_1=0^\circ$; $\Phi=0^\circ-90^\circ$; $\phi_2=30^\circ$, denoted as 1, see the dotted line in Fig. 7a) and $\{1\ 1\ -2\ 9\}\langle uv\ tw \rangle$ fiber ($\phi_1=0^\circ-90^\circ$; $\Phi=20^\circ$; $\phi_2=30^\circ$, denoted as 2, see the dotted line in Fig. 7a) with some dominant components. Those fibers and components are maintained after annealing, yet their scatter is increased and their intensity is significantly decreased. The development of the ODF intensities along the main texture fibers as a function of the annealing time is presented in Fig. 7c. In the $\langle 1\ 0\ -1\ 0 \rangle$ fiber as the annealing time is increased, there is a continuous reduction of the intensity of this fiber. There is a slight increase in the ODF intensity in the surrounding of the main texture component $(7\ 7\ -14\ 27)\langle -1\ -1\ 0\ 0 \rangle$ as the sample is annealed at 370°C for 30 s. There is also another peak in the surrounding of the $(8\ 8\ -16\ 15)\langle -1\ -1\ 0\ 0 \rangle$ texture component. Both texture components are rather stable and the intensity of both of them weakens during extended annealing times. In the case of the $\{1\ 1\ -2\ 9\}\langle uv\ tw \rangle$ fiber, the intensity of its main texture component $(1\ 1\ -2\ 9)\langle -1\ -2\ 3\ 1 \rangle$ also weakens and its scatter increases. These results also exhibit the weakening of the texture fibers and components during annealing rather than the evolution of a different recrystallization texture.

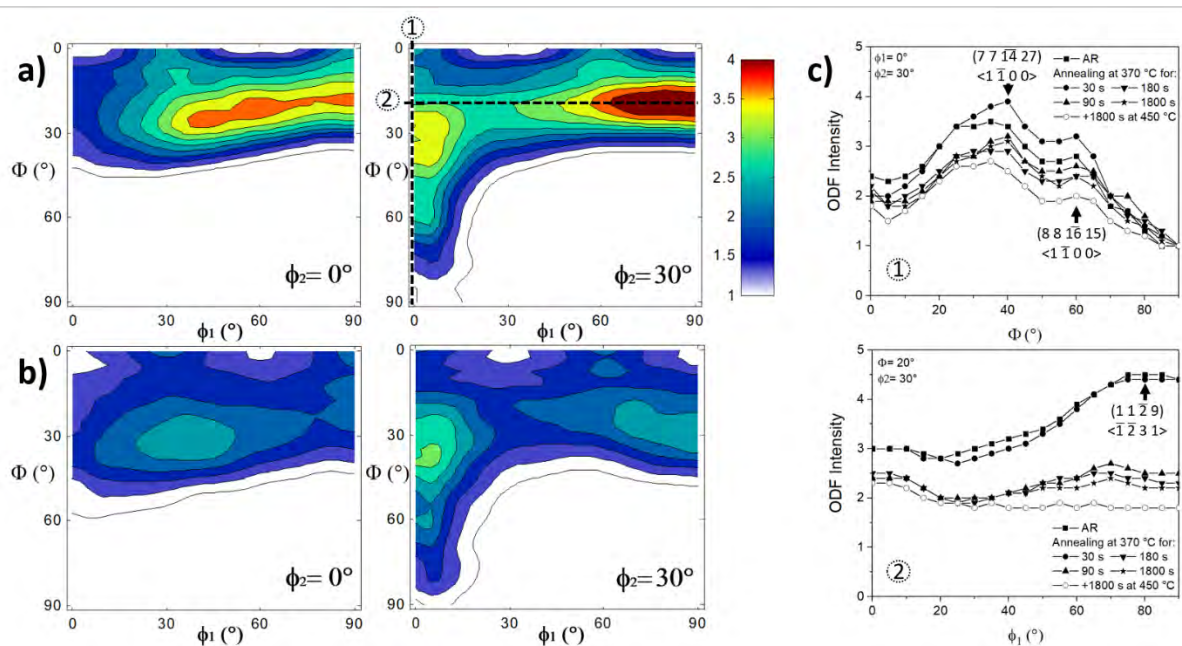


Fig. 7 Texture representation in terms of ODF sections ($\varphi_2=0^\circ$ and $\varphi_2=30^\circ$) plotted with orthotropic symmetry for a) as-rolled sheet, b) annealed sample at 370 °C for 1800 s and c) ODF intensity plots for marked fibers denoted as “1” and “2” (see dotted lines in Fig. 7a) for the whole set of annealed samples.

3.3 *Ex-situ* EBSD measurements

To uncover more details of the microstructure-texture evolution in the Mg-Zn-Ca-Zr alloy during the early annealing stage, *ex-situ* EBSD measurements were performed. The orientation image (OI) maps and their respective local texture after different annealing times are presented in Fig. 8. In general, the microstructural development of the *ex-situ* annealing shows a good agreement to the microstructural evolution of the bulk material. Similarly, there is agreement with regard to the texture evolution, where the RD-split texture components weaken significantly making visible the TD-split peaks. In addition, it is seen that the texture retains the $\langle 1\ 0\ -1\ 0 \rangle$ component parallel to RD. Likewise, the ODF plots calculated from the *ex-situ* experiments show excellent correlation to those obtained by XRD (see supplementary Fig. S2). A careful inspection of the OI maps reveals that during annealing some of the deformation twins shrink and eventually disappear (see the white filled arrows in Fig. 8 a-c), while some grains are stable during the whole annealing process (see black filled arrows in Fig. 8 a-d).

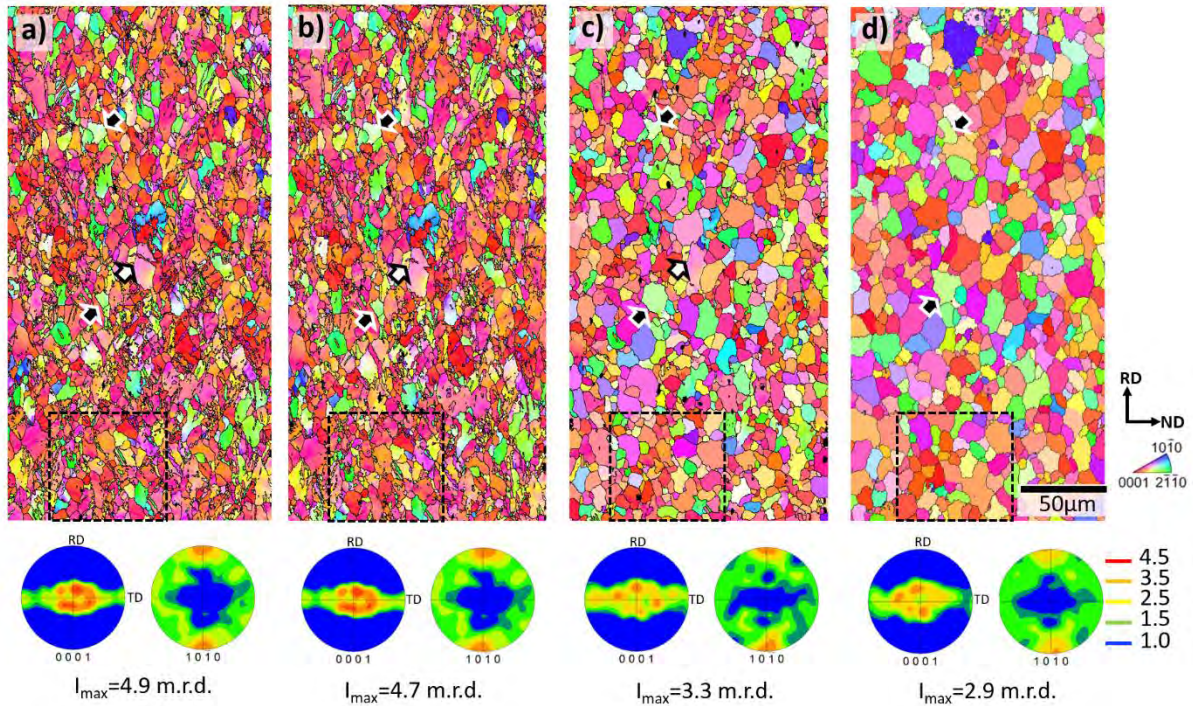


Fig. 8 *Ex-situ* EBSD orientation image maps (OI) and related local texture in terms of the (0 0 1) and (1 0 -1 0) pole figures of a) hot rolled sample and after annealing at 350 °C for b) 270 s, c) 570 s and d) 1800 s.

From the microstructure development presented in Fig. 8, it is evident that many of the green colored grains with *c*-axis largely tilted from ND to TD are stable during annealing. Eventually, they can develop a recrystallized morphology at the end of the annealing process. This has also been reported for a conventional AZ31 alloy, where grains with largely tilted *c*-axis from ND to TD revealed signs of extended recovery [28, 29]. The development of this type of “green” grains shows noticeable similarities to the development of the “white” grains in Ti alloys, which are stable during recrystallization annealing [30]. To provide a more quantitative analysis of the contribution of certain fractions of grains to the microstructure and texture development, grains with a deviation of their *c*-axis from ND to RD and TD, respectively, were separately evaluated. The fraction of grains with their *c*-axis close to ND (ND deviation from

0-30°), intermediate (ND deviation from 30-60°) and largely tilted grains (ND deviation from 60-90°) are presented in Fig. 9. To evaluate changes in the relative fraction of each type of grains, the same area was evaluated in the as-rolled condition (Fig. 9a) and after annealing at 350 °C for 1800 s (Fig. 9b). In good agreement with the intensity plots shown above, Fig. 6, the EBSD measurements revealed the decrease in the area fraction of grains along RD (0-30°) from 24 % in the as-rolled condition to 13 % after annealing. Interestingly, there is the clear development of grains with their *c*-axis tilted towards RD in the range of 30-60° from an initial area fraction of 11 % to 21 %. Largely tilted grains towards RD (ND deviation from 60-90°) do not show any significant change and the area fraction remain close to 1 %. With respect to grains with their *c*-axis tilted towards TD, the fraction of grains in the range of 0-30° show also a decrease from 17 % in the as-rolled state to only 12 % after annealing. The fraction of intermediate tilted grains towards TD in the range of 30-60° (in the range of the characteristic TD-split) remains almost unchanged. There is a subtle decrease in the area relative fraction of this type of grains from 34 % in the as-rolled state to 33 % after annealing. On the other hand, it is possible to see the development of grains with largely tilted *c*-axis towards TD (ND deviation from 60-90°). The fraction increases from 13 % in the as-rolled condition to 20 % after annealing. This correlates well with the continuous increase in the texture intensity of the corresponding orientations, i.e. TD-split orientation in the range from 65-90°, as shown in Fig. 6.

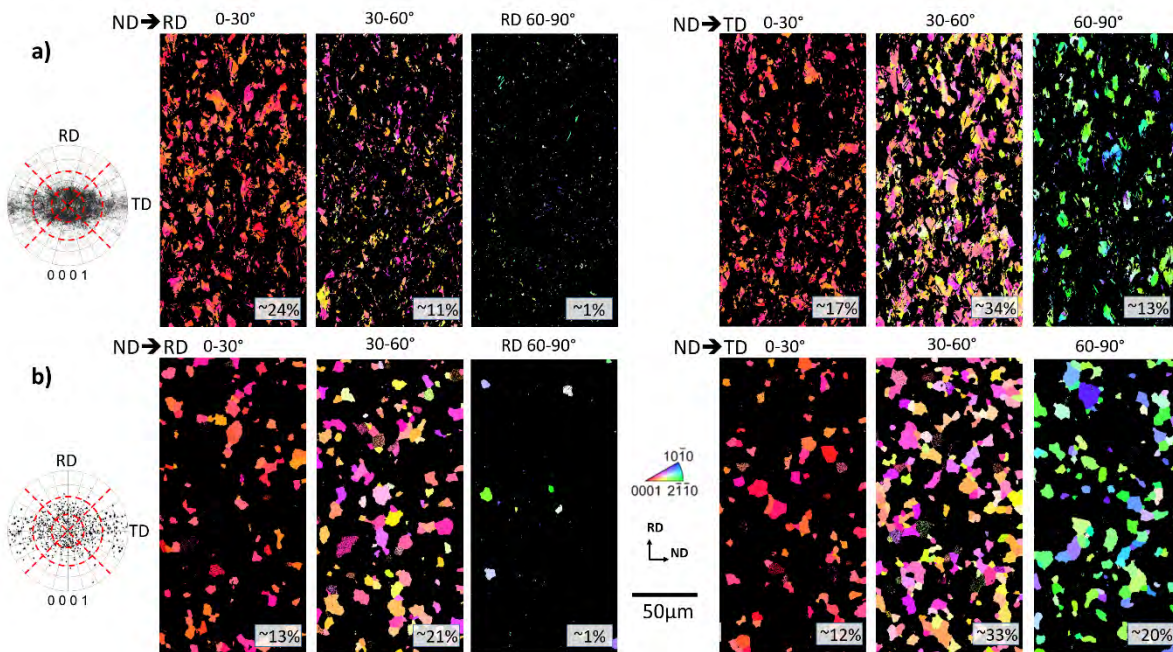


Fig. 9 Discrete (0 0 0 1) pole figure showing orientations corresponding to grains with c -axis deviating from ND to different ranges, i.e. $0^\circ < \text{ND deviation} \leq 30^\circ$, $30^\circ < \text{ND deviation} \leq 60^\circ$ and $60^\circ < \text{ND deviation} \leq 90^\circ$, towards RD and TD, respectively. a) As-rolled sample and b) sample annealed at 350 °C for 1800 s.

3.4 Mechanical properties

Fig. 10 plots the true stress - true strain curves of samples in as-rolled and annealed states, i.e. annealing at 370 °C for 30, 90 and 1800 s. The corresponding tensile properties are listed in Table 1. The as-rolled sample shows a high strength in all sheet planar directions. The ductility along 45° and TD is relatively high for a strain-hardened Mg alloy with elongations around 20 %, while the ductility along the RD is low, Fig. 10a. After 30 s annealing, the sheet shows an increase in ductility along RD without losing strength, Fig. 10b. After 90 s of annealing, there is a significant decrease in strength in all testing directions. The flow curves of the 90 s annealed samples show the concave down shape, which can be linked with the high twinning activity at the beginning of the deformation followed by a rapid increase in the

strength during tensile straining. The 1800 s annealed samples show a noticeable increase in the fracture strain along RD, which correlates well with the monotonic increase of its n-value. Moreover, there is a further decrease in strength in all testing directions. It is to note that the mechanical behavior is similar to the counterpart samples annealed for only 90 s. In addition, it is important to highlight the almost negligible changes in the r-values in all testing conditions. Although, the mechanical properties of the annealed material at 370 °C for 1800 s are slightly higher than recrystallized sheets made out of Mg-Zn-Ca and Mg-Zn-Ce [12, 13], based on the similar textures and grain sizes, there is a very good agreement in the mechanical behavior and anisotropy with those alloys.

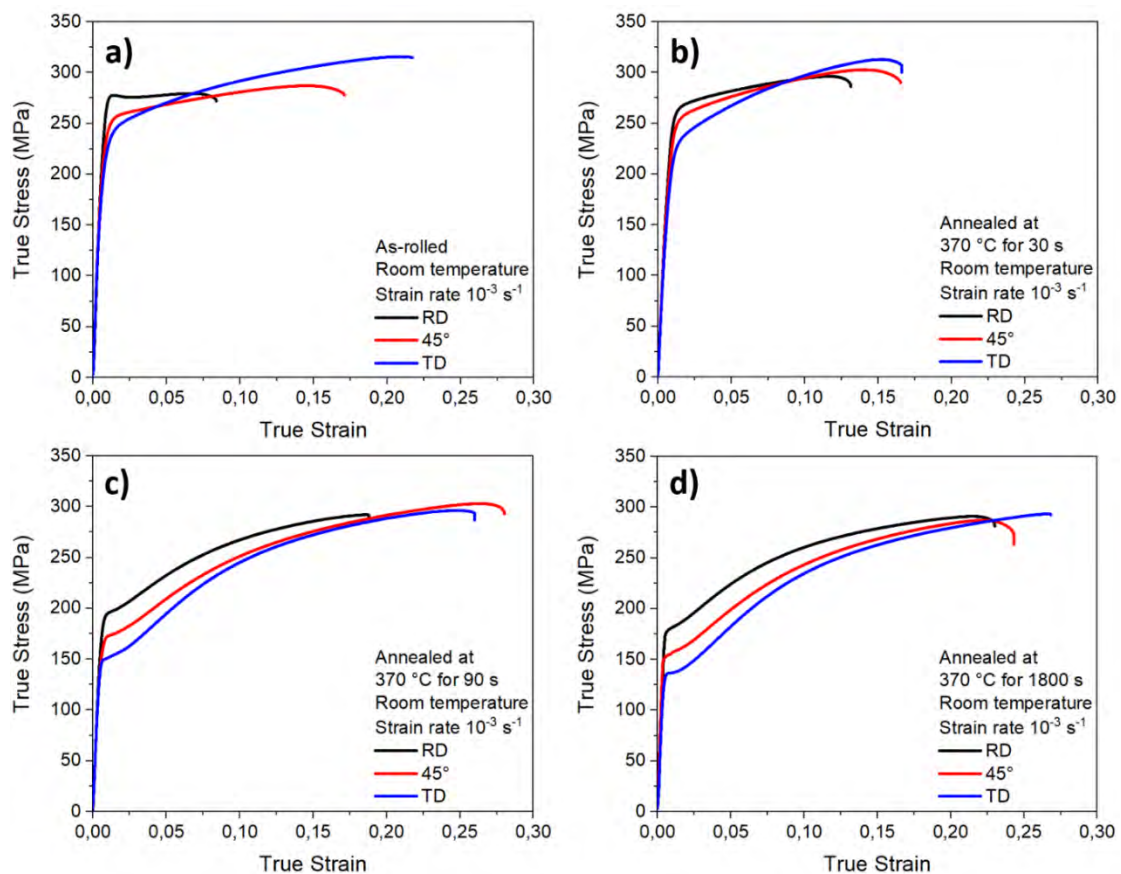


Fig. 10 True stress-true strain curves of a) as-rolled, b-d) samples annealed at 370 °C for 30, 90 and 1800 s, respectively.

Table 1 Tensile properties at room temperature of as-rolled and annealed samples tested along RD, 45 ° to RD and TD (YS, tensile 0.2% yield stress; UTS, ultimate tensile stress, ϵ_u , uniform elongation; ϵ_f , elongation to fracture, n-value and r_{10} Lankford parameter).

		YS (MPa)	UTS (MPa)	ϵ_u (%)	ϵ_f (%)	n-value	r_{10} -value
As-rolled	RD	255±2	276±2	1	8	---	---
	45°	217±3	255±2	5	19	0.04±0.01	1.2±1*
	TD	200±2	265±2	12	23	0.09±0.01	0.7±0.1
Annealed 370 °C for 30 s	RD	238±4	270±4	5	13	0.05±0.01	1.0±0.1*
	45°	211±4	264±3	10	17	0.08±0.01	1.3±0.1
	TD	195±3	268±4	13	17	0.13±0.01	1.0±0.1
Annealed 370 °C for 90 s	RD	186±2	246±4	15	20	0.18±0.01	0.9±0.1
	45°	160±3	237±2	20	31	0.23±0.01	1.2±0.1
	TD	146±3	235±2	20	30	0.28±0.01	0.9±0.1
Annealed 370 °C for 1800 s	RD	174±3	239±3	16	25	0.19±0.01	0.9±0.1
	45°	152±3	232±2	19	27	0.25±0.01	1.1±0.1
	TD	135±2	226±2	21	31	0.30±0.01	0.8±0.1

* r -value measured at 5 % ϵ_u

4. Discussion

It has been shown from the diverse microstructural analysis that the Mg-Zn-Ca-Zr alloy exhibits a consistent texture development during all processing steps. Namely, the deformed TRC-strip and rolled sheet show a strong deformation texture with a double peak of tilted basal poles towards RD (RD-split) and a broad scatter of basal poles towards TD. After annealing, there is an obvious weakening of the texture in both of them. However, the recrystallization texture of the rolled samples can develop the distinctive TD-split of the basal poles.

It is shown by annealing experiments that such development is not necessarily the result of the distinctive development of grains with basal poles tilting ~35 ° from ND towards TD, but

related with the overall weakening of the texture intensity and the persistence of grains having the corresponding orientations. The *ex-situ* EBSD analysis shows a noticeable increase in the area fraction of the grains with specific orientations, i.e. tilted basal poles along RD in the range of 30-60° and tilted basal poles along TD in the range of 60-90°, after annealing.. From the present results; it is assumed that the texture weakening can be linked to the nucleation and growth of grains with those orientations.

In the following sections, the discussion focuses on aspects of the recrystallization mechanisms and their relationship with the deformation mechanisms.

4. 1. Recrystallization mechanisms

According to the microstructural and texture changes of the as-rolled condition upon annealing, two main features are considered in the present study. The first one is the transition of the main texture components from the RD-split peaks to TD-split peaks, while the $\langle 1\ 0\ -1\ 0 \rangle$ poles parallel to RD are retained without rotation or weakening. This component is still parallel to RD even after a significant grain growth (see supplementary Fig. S3). The second aspect is the growth of recovered grains by consuming the neighboring deformed grains. As the growth of recovered volumes proceeds, a recrystallized-like structure is developed. To track the microstructure evolution more precisely, a representative area was investigated in high magnification. The microstructure of the selected area is shown in Fig. 11, which corresponds to hatched rectangles in Fig. 8. Fig. 11 presents the different fractions of the microstructure according to the internal grain orientation spread (GOS) and kernel average misorientation (KAM) maps as an indication of the regions with high stored strain. The grains with $GOS < 0.5^\circ$ are considered as recrystallized. This is based on their low internal misorientation degree, whereas the remaining fraction of the microstructure is considered as

recovered or deformed grains. The KAM maps in the present study are calculated according to the degree of misorientation between a kernel (measuring point) and its third neighbors [31]. Microstructure evolution of 10 selected grains with different orientations is discussed in the context of Fig. 11. In the as-rolled condition (see Fig. 11a), a careful microstructure examination revealed that only grains 3 and 8 originate from “well-defined” recrystallization sites. Grain 3 and grain 8 show a visible growth during the annealing. The facts that those grains are identified in the OI map for grains with $GOS < 0.5^\circ$ and the size of about $\sim 1 \mu\text{m}$ in the as-rolled condition, allow us to assume that they originate from the growth of a recrystallization nuclei. Several small recrystallized grains with different orientations are also observed, but most of them are consumed by other growing grains. The rest of the microstructure clearly shows a recovery process. This is identified by a large number of low angle boundaries in the grains with $GOS > 0.5^\circ$ and high stored strain as shown in the KAM maps. The orientations of the grain 3 and grain 8 after complete recrystallization are revealed in a discrete (0 0 0 1) pole figure presented in Fig. 12. The development of grains with these orientations definitely contribute to the formation or strengthening of the TD-split texture component. As a possible origin of such “well-defined” recrystallization nuclei, the activation of $\{1\ 0\ -1\ 1\}$ - $\{1\ 0\ -1\ 2\}$ secondary twins has to be considered [11, 29, 32]. Recently, it has been shown that recrystallized grains originating from secondary twins can give rise to the formation of the characteristic TD-split texture in WE43 alloy [11]. That finding also is in good agreement with observations of the texture development of cold rolled commercially pure Ti, where the intensive activity of secondary twins is related to the concomitant formation of the TD-split texture [33, 34]. Fig. 13 exhibits image quality (IQ) maps of the as-rolled and annealed samples for 270 s and 570 s at 350 °C. Those IQ maps correspond to the same magnified areas presented in Fig. 11 a-c. In those maps, the superposition of twin boundaries shows that the

nucleation sites of the grain 3 and grain 8 are located within $\{1\ 0\ -1\ 1\}$ - $\{1\ 0\ -1\ 2\}$ secondary twin volumes, as indicated in the dotted circles in Fig. 13a-b. Other $\{1\ 0\ -1\ 1\}$ - $\{1\ 0\ -1\ 2\}$ secondary twins also develop a grain structure retaining the twin boundary as indicated by the white filled arrows in Fig. 13 a-c. Consequently, the development of those grains can be related to the activation of discontinuous static recrystallization (dSRX) [35, 36]. On the other hand, as seen in Figs. 11 a-d and corresponding orientation plotted in Fig. 12, the origin of the remaining selected grains is related to recovered volumes within deformed grains. For instance, grain 10 develops from a small-recovered volume that grows and consumes the deformed neighboring grains. This can clearly be seen in the development of grain 10 as indicated by the white arrow in the OI and KAM maps in Fig. 11c. As grain 10 continues to grow, it eventually meets other grains with similar orientations. This leads to the formation of a low angle grain boundary, e.g. with grain 9. The rest of the analyzed grains show similar features. The orientations of all these grains, Fig. 12, show similarities with the orientations contained in the deformed state. The findings described above can provide proof that continuous static recrystallization (cSRX), also known as extended recovery was active during the annealing process. Contrarily to the discontinuous recrystallization cases of grains 3 and 8, the initial volume of the rest of the analyzed grains (including grain 10) could not be identified in the $GOS < 0.5^\circ$ map of the as-rolled condition. Therefore, extended recovery had to occur during the first seconds of subsequent annealing. The controlling mechanism behind the development of those grains, special emphasis on grain 10, seems to be strain induced boundary migration (SIBM). As shown in Fig. 11c, the white filled arrow clearly shows the growing path of grain 10. The present result show similarities to the mechanism described in [37]. It is to mention that the recrystallization behavior of this Mg alloy shows resemblances

with the primary recrystallization mechanisms observed in other hexagonal metal e.g. Zr-2Hf alloy, where extended recovery also plays an important role [23].

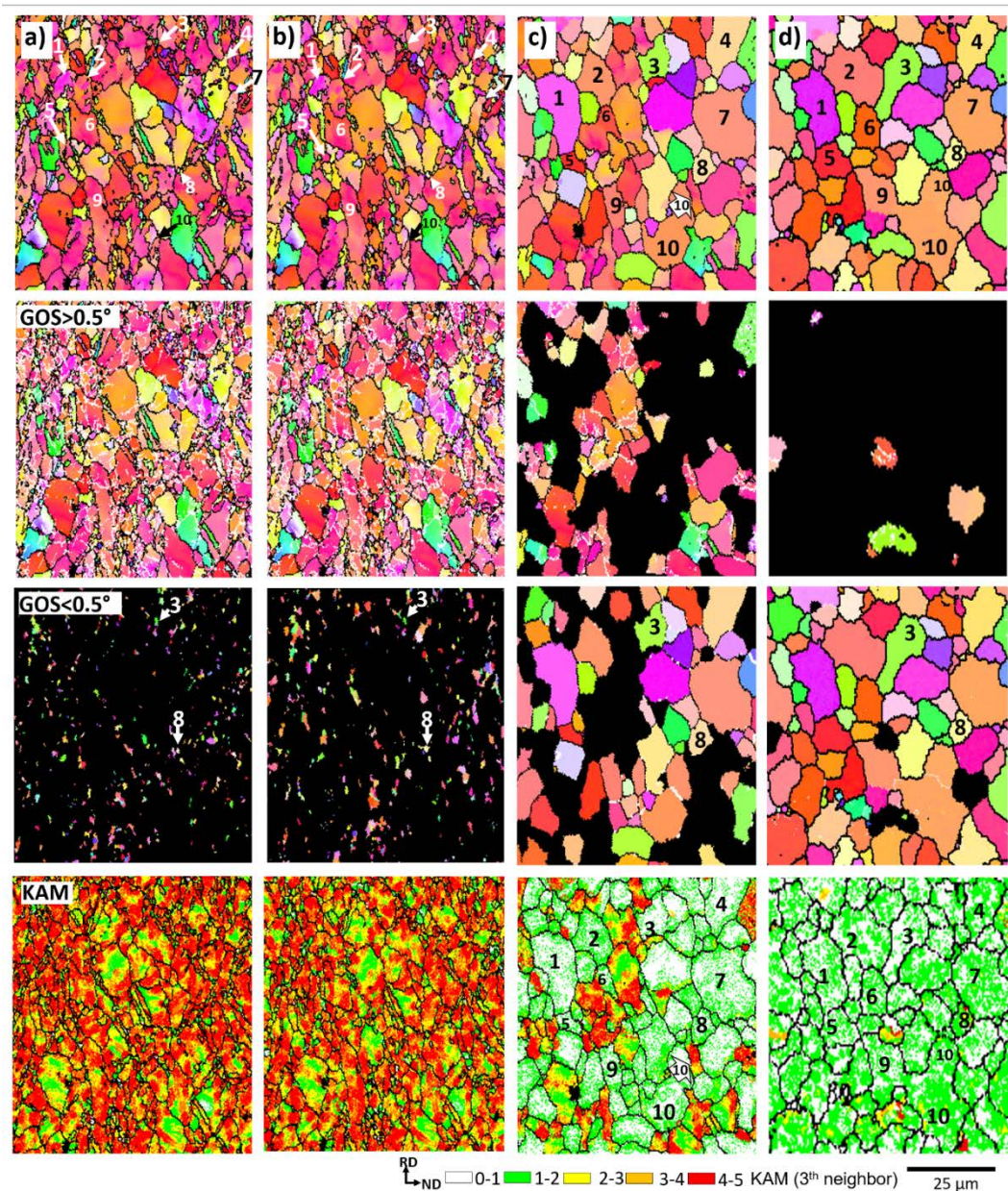


Fig. 11 *Ex-situ* EBSD OI maps, fractions of the deformed ($GOS > 0.5^\circ$) and recrystallized ($GOS < 0.5^\circ$) fractions of the microstructure with corresponding KAM maps of a) as-rolled sample, b) sample annealed 270 s, c) sample annealed 570 s, and d) sample annealed 1800 s at 350 °C. In black: high angle grain boundaries ($\theta > 15^\circ$) and in white: low angle grain boundaries ($2^\circ < \theta < 14^\circ$).

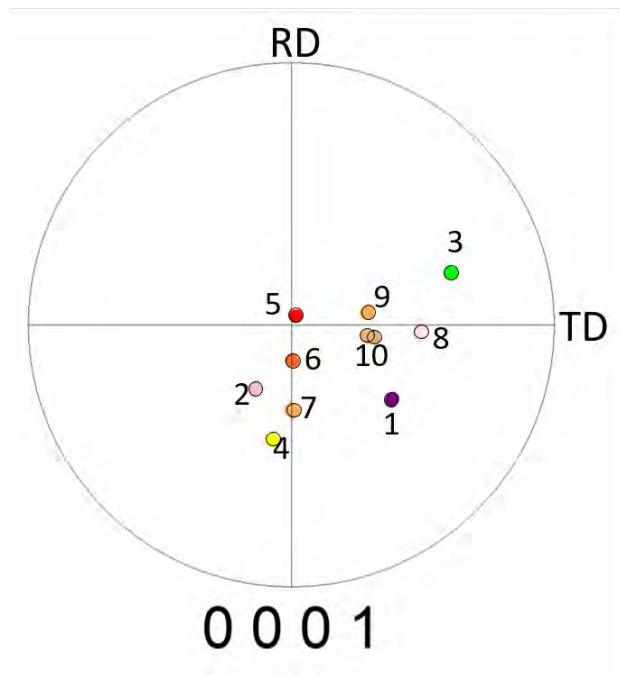


Fig. 12 Discrete (0 0 0 1) pole figure showing the orientation of 10 selected grains depicted in Fig. 11.

4.2. Deformation mechanisms and their relationship to microstructure development

So far, it has been shown that both dSRX and extended recovery are active, and that the latter appears to be the dominant mechanism for microstructure development during annealing. It has also been revealed that $\{1\ 0\ -1\ 1\}$ - $\{1\ 0\ -1\ 2\}$ double twinned volumes act as preferential sites for recrystallization, e.g. grains 3 and 8 in Fig. 11. Even so, it is also necessary to examine the relationship of different deformation mechanisms, i.e. other twinning modes and dislocation slip with recrystallization.

4.2.1 Deformation twins

The importance of $\{1\ 0\ -1\ 1\}$ - $\{1\ 0\ -1\ 2\}$ secondary twins was described in previous works for the development of the TD-split texture in WE43 Mg alloy and for other Mg-RE alloys [11, 32, 36]. It was shown systematically via *quasi in-situ* EBSD [11] and 3D-EBSD [38], that the

preferential nucleation sites are double twin-double twin intersections and double twins at grain boundaries. Recrystallized grains triggered at such intersections can grow readily into the parent grains and subsequently to neighboring deformed grains.

As sites suitable for recrystallization, not only the sequence $\{1\ 0\ -1\ 1\}$ - $\{1\ 0\ -1\ 2\}$ double twins, but also single $\{1\ 0\ -1\ 1\}$ contraction twins [39] and $\{1\ 0\ -1\ 2\}$ - $\{1\ 0\ -1\ 1\}$ twins can lead to the development of new recrystallized grains [40]. Experiments using pure Mg single crystals deformed at room temperature under plane strain compression (PSC) along the $\langle 1\ 1\ -2\ 0 \rangle$ direction have exposed that the activation of $\{1\ 0\ -1\ 1\}$ contraction within primary $\{1\ 0\ -1\ 2\}$ extension twins can also serve as a nucleation site for dynamically recrystallized grains [40]. The mechanism behind the $\{1\ 0\ -1\ 1\}$ contraction twin fragmentation and eventual dynamic recrystallization (DRX) was associated with the lattice rotation of the twinned volume around the c -axis by prismatic $\langle a \rangle$ slip. This leads to a precursor stage to DRX, where self-diffusion and dynamic recovery are strongly promoted in the fragmented twin bands. Such non-planar movement of dislocations is essential for the formation of a three-dimensional dislocation structure.

In the present study, single $\{1\ 0\ -1\ 1\}$ contraction twins do not show evidence of static recrystallization. As indicated by the black filled arrows in Fig. 13, several $\{1\ 0\ -1\ 1\}$ contraction twins vanish upon annealing. Some other $\{1\ 0\ -1\ 1\}$ contraction twins remain stable during the early annealing stage and are eventually consumed by other growing grains. Therefore, the importance of those twins is to serve as a volume to be $\{1\ 0\ -1\ 1\}$ - $\{1\ 0\ -1\ 2\}$ secondary twins leading to the mechanism described above.

With regard to extension twins, it has been shown in [40] that single, double or even tertiary generation of $\{1\ 0\ -1\ 2\}$ extension twins do not tend to recrystallize dynamically. In the case

of SRX, $\{1\ 0\ -1\ 2\}$ extension twins are not considered as possible sites of primary recrystallization and are normally consumed by adjacent recrystallized grains during their growth stage [11]. Although, the presence of the uncommon extension twinning mode $\{1\ 1\ -2\ 1\} \langle -1\ -1\ 2\ 6 \rangle$ (normally found in Ti and Zr which can reorient the crystal lattice approximately 34° about the $\langle 1\ 0\ -1\ 0 \rangle$ direction) has been reported for Mg WE43 in ref. [41], its significance as a recrystallization sites is still unclear. In this work, this twinning mode was also investigated and less than 1% of the total fraction of the microstructure is covered by this twinning mode, making the influence of this type of twins on the recrystallization behavior difficult to evaluate. On the other hand, it is found that the origin of grain 10, see Fig 13a-b indicated by the white circles, lies in a deformed grain where a $\{1\ 0\ -1\ 2\}$ extension twin had been operative. At this stage, it is hard to properly identify the whole twin boundary and distinguish the matrix from the twin volume. This is due to the advanced recovery process, even in the as-rolled state despite the rapid cooling. As seen in Fig. 13d, the misorientation in the twinned region corresponds to the common $[1\ 1\ -2\ 0]$ rotation axis with a rotation angle of 86° confirming the $\{1\ 0\ -1\ 2\}$ extension twinning mode. To the best knowledge of the present authors, this is the first time that a link between the remaining matrix-grain (more likely) or the twinned volume with recrystallization is presented. In the present case, the development of the recrystallized-like volume is related to extended recovery. Therefore, the original orientation (belonging to the TD –split texture) is maintained after annealing. Although, at this point, it might seem to be an isolated case, recent hot PSC experiments using the same alloy show that in the deformed matrix of grains containing $\{1\ 0\ -1\ 2\}$ extension twins nucleation of new grains is feasible. Those recovered volumes, consequently, can inherit the TD-split texture component.

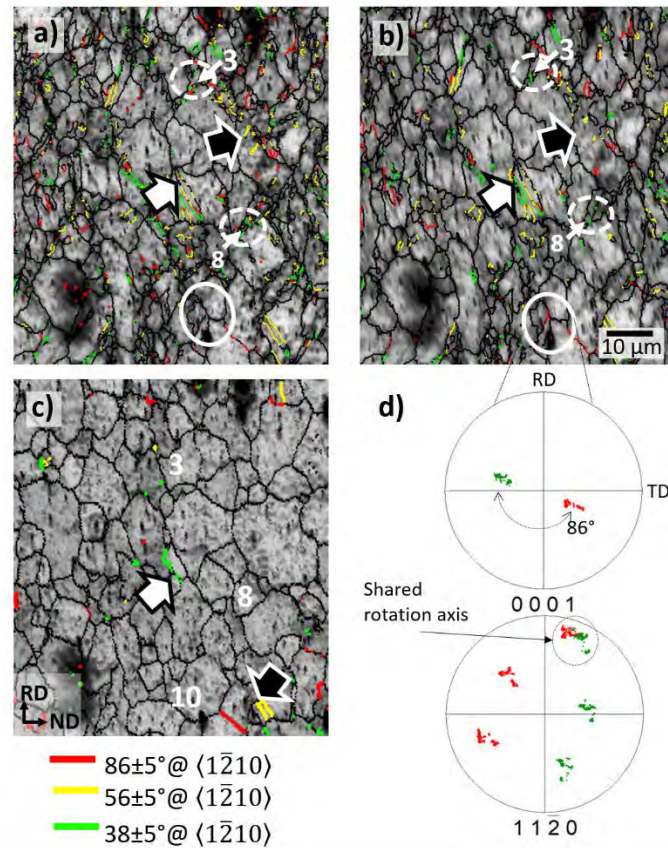


Fig. 13 *Ex-situ* image quality (IQ) maps from magnified images from areas marked in Fig. 8 for a) as-rolled sample, b) sample annealed 270 s and c) sample annealed at 350 °C for 570 s, and d) corresponding (0 0 0 1) and {1 1 -2 0} pole figures showing orientations of a deformed grain and related twin volume. In black: high angle grain boundaries ($\theta > 15^\circ$), in red: {1 0 -1 2} extension twins, in yellow: {1 0 -1 1} contraction twins and in green: {1 0 -1 1}-{1 0 -1 2} double twins. (For interpretation of the references to colour in this figure legend, the reader is referred to the web version of this article).

4.2.2. Dislocation slip

To infer what kind of slip mode could have participated during rolling, the distribution of in-grain misorientation axis (IGMA) for different sets of grains was examined. The principle of IGMA is based on slip induce lattice rotation and the determination of its rotation axis [42,

43]. The IGMA method considers that the observed misorientation arises from a bending of the crystal lattice under the action of slip. Such bending takes place about an axis, i.e. Taylor axis, which gives rise to a lattice rotation. The Taylor axis is at a crystallographic direction lying in the slip plane and perpendicular to the slip direction and is defined as follows:

$$T_s = n_s \times d_s \quad (2)$$

where T_s , n_s and d_s are the Taylor axis, slip plane and slip direction for a given slip mode s , respectively. This allows to determine the dominant slip mode in a deformed single crystal by matching the Taylor axis for a given slip mode to the experimentally measured IGMA. More details on the theoretical description of IGMA and Taylor axis for different slip modes are found elsewhere [39, 40]. By using EBSD data as described in ref. [44], the misorientation within some selected grains are considered. There are two important assumptions, the first being that those misorientations are a result of remaining geometrically necessary dislocations. The second is that many dislocations had already been absorbed into grain boundaries or annihilated by recovery. Therefore, some dislocations cannot be further characterized. In the present paper, similarly to the description in ref. [44], we also look for tendencies of a large number of IGMA measurements for different sets of interesting crystallographic orientations rather than looking for an accurate IGMA value for individual points. The results of IGMA analysis for an average misorientation of 4° (angular range 2 to 6°) are presented in Fig. 14. For clarity, the as-rolled OI map and the discrete (0 0 0 1) pole figures corresponding to the IGMA analysis are replotted in Fig. 14a. The IGMA distribution plots for largely tilted c -axis grains, lying almost parallel to TD as shown in discrete pole figure in Fig. 14b, shows a slight higher concentration of preferred misorientation axis close to [0 0 0 1]. This suggest that prismatic $\langle a \rangle$ slip was slightly more dominant. The dominance of

prismatic $\langle a \rangle$ slip is more evident for the grains having orientations close to the TD-split texture component, Fig. 14c. With respect to grains with orientations tilted from ND towards RD, they also show misorientation axis close to $[0\ 0\ 0\ 1]$, as well as a subtle trend of misorientation axis along the arc between $\langle 1\ 0\ -1\ 0 \rangle$ and $\langle 1\ 1\ -2\ 0 \rangle$ (See Fig. 14d). This suggests a more balanced activity of multiple slip. For the grains with c -axis parallel to ND, the trend is to misorientations axis lying along the arc between $\langle 1\ 0\ -1\ 0 \rangle$ and $\langle 1\ 1\ -2\ 0 \rangle$. This indicates the predominance of dislocations produced by basal $\langle a \rangle$ or pyramidal $\langle c+a \rangle$ slip. Because basal $\langle a \rangle$ and pyramidal $\langle c+a \rangle$ slip share the same Taylor axis, a differentiation between these two slip modes is not possible from the IGMA analysis. Nevertheless, due to the high rolling temperature used in this work, the activity of pyramidal $\langle c+a \rangle$ slip is expected. As another possible slip mode, the $\langle 1\ 0\ -1\ 2 \rangle$ Taylor axis for pyramidal $\langle a \rangle$ slip is also depicted in the IGMA distribution plots. Although it is difficult to see a clear trend for this slip mode, it is considered based on the high probability to be thermally activated during rolling. Moreover, in recent publications, the combined activity of pyramidal $\langle a \rangle$ with basal $\langle a \rangle$ and prismatic $\langle a \rangle$ slip has been observed during tensile deformation of binary Mg-Y alloy at room temperature or predicted by simulations to be operative during tensile deformation of Mg-Zn-RE-Zr alloys [45-47]. In addition to this, the large presence of secondary phase particles (c.f. Fig. 2, mainly Mg_2Ca and some $\text{Mg}_6\text{Zn}_3\text{Ca}_2$) could also enhance the activation of non-basal dislocations, mainly by hardening soft slip modes and twins, and/or by locking dislocation due to precipitation [41, 48, 49]. Therefore, pyramidal slip modes are considered in the present paper. The simultaneous activation of different deformation modes is very important. The activation of different slip modes could lead to the formation of the 3D recrystallization nuclei, consequently, triggering the recrystallization process more efficiently. This fact correlates well with the enhanced recrystallization that occurred in grains with c -axis tilted

from ND to RD. Especially in the range from 30-60° *c*-axis tilting from ND to RD. In this range, the increase in the recrystallized fraction of the microstructure showed the highest value (c.f. Fig. 9). For the deformed grains having their *c*-axis tilted towards RD, not only prismatic $\langle a \rangle$ slip but also basal $\langle a \rangle$ and/or pyramidal $\langle c+a \rangle$ slip were activated in a more balanced way as revealed by the IGMA plot in Fig. 14d. On the other hand, the preferential activation of a dominant slip system, e.g. prismatic $\langle a \rangle$ slip, as revealed by the IGMA plot in Fig. 14c for the TD-split oriented grains, could lead to enhanced recovery reactions. This correlates well with the fraction of grains belonging to the TD-split texture, where the “recrystallized” fraction remains virtually unchanged with respect to the fraction of deformed grains (c.f. Fig. 9). For instance, it has been observed that highly deformed Zn crystals via prismatic $\langle a \rangle$ slip tend only to recover without signs of recrystallization [50]. Therefore, it can be hypothesized that extended recovery plays an important role in the microstructural development during annealing, especially for grains with *c*-axis tilted away from ND to TD where prismatic slip was more dominant. Further analysis and crystal plasticity simulations on the activities of these slip modes are to be provided in the context of hot PSC experiments in a future work.

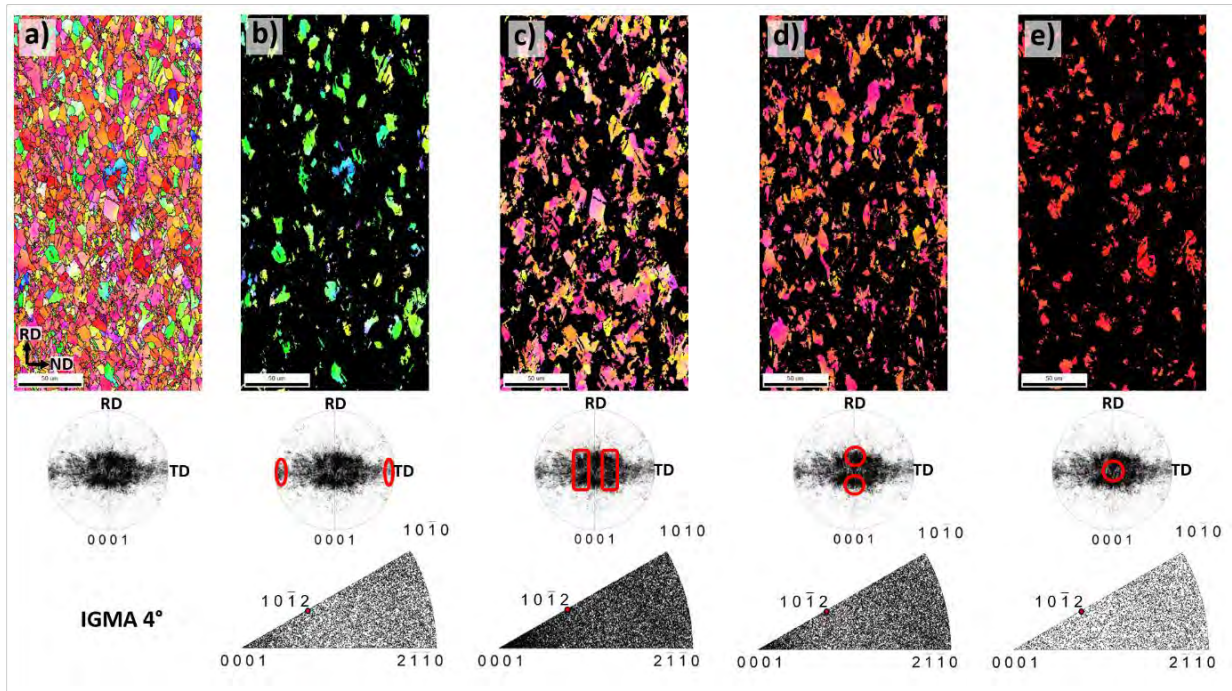


Fig. 14 a) OI maps and respective discrete (0 0 0 1) pole figure showing the whole set of orientations, b-e) OI maps, respective discrete pole figure and IGMA distribution plots for different sets of grains divided according to their orientation.

Summary

In the present work, a systematic investigation of the microstructure-texture development during the primary recrystallization behavior of a hot rolled TRC-Mg-Zn-Ca-Zr alloy is provided. The results from X-ray measurements coupled with optical and *ex-situ* EBSD microstructural analysis allow us to draw the following conclusions:

A characteristic development of the RD-split texture towards the TD-split texture during static recrystallization has been observed. The development of the distinctive TD-split texture is strongly related to the weakening of the overall texture intensity, rather than the nucleation and growth of grains with tilted TD orientations. It is demonstrated that such stable

orientations are already contained in the deformed state and can persist during recrystallization annealing.

During recrystallization annealing dSRX and extended recovery mechanisms are active. Nucleation and growth of grains within $\{1\ 0\ -1\ 1\}$ - $\{1\ 0\ -1\ 2\}$ double twins, related to the development of TD orientations, promote the activation of the former type of recrystallization mechanism. On the other hand, the development of most of the “recrystallized” grains seem to be dominated by extended recovery reactions where SIBM is the controlling mechanism.

The development of stable orientations, which allow the TD-split texture components to be visible after annealing, is related with the dominance of prismatic $\langle a \rangle$ slip. Grains within the TD-split texture components can be twinned developing a mirror orientation. In this regard, it has been shown that extended recovery of deformed grains containing $\{1\ 0\ -1\ 2\}$ extension twins can occur. In this case, the recovered volume will inherit the original orientation of the deformed grain with the corresponding TD-split orientation.

Acknowledgments

The fruitful discussion with Dr. Nowfal Al-Hamdany and the technical assistance of Petra Fischer, Yukyung Shin and Alexander Reichert at Helmholtz-Zentrum Geesthacht are gratefully acknowledged. This work was partially financed by Volkswagen AG and POSCO-Korea.

Data availability: The raw/processed data required to reproduce these findings cannot be shared at this time as the data also forms part of an ongoing study.

References

1. Y. Chino, M. Kado, M. Mabuchi, Enhancement of tensile ductility and stretch formability of magnesium by addition of 0.2 wt% (0.035 at%) Ce, *Mater. Sci. Eng. A* 494, 2008, 343-349
2. S. Sandlöbes, M. Friák, S. Korte-Kerzel, Z. Pei, J. Neugebauer, D. Raabe, A rare earth free magnesium alloy with improved intrinsic ductility, *Sci. Rep.* 7:10458, 2017, 1-8
3. T.Al-Samman, X. Li, Sheet texture modification in magnesium based alloys by selective rare earth alloying, *Mater. Sci. Eng. A* 528, 2011,3809-3022
4. S. Sandlöbes, S. Zaefferer, I. Schestakow, S. Yi, R. Gonzalez-Martinez, On the role of non-basal deformation mechanisms for the ductility of Mg and Mg-Y alloys, *Acta Mater.* 59, 2011, 429-439
5. S. Sandlöbes, M. Friák, S. Zaefferer, A. Dick, S. Yi, L. Letzig, Z. Pei, L.F. Zhu, J. Neugebauer, D. Raabe, The relation between ductility and stacking fault energies in Mg and Mg-Y alloys, *Acta Mater.* 60, 2012, 3011-3021
6. S. Yi, J. Bohlen, F. Heinemann, D. Letzig, Mechanical anisotropy and deep drawing behavior of AZ31 and ZE10 magnesium alloy sheets, *Acta Mater.* 58, 2010, 592-605
7. L.W.F. Mackenzie, M.O. Pekguleryuz, The recrystallization and texture of magnesium-zinc-cerium alloys, *Scripta Mater.* 59, 2008, 665-668
8. J. Bohlen, M.R. Nürnberg, J.W. Senn, D. Letzig, S.R. Agnew, The texture and anisotropy of magnesium-zinc-rare earth alloy sheets, *Acta Mater.* 55, 2007, 2101-2112

9. L. Liu, X. Chen, F. Pan, S. Gao, C. Zhao, A new high strength Mg-Zn-Ce-Y-Zr magnesium alloy, *J. Alloys Compd.* 688, 2016, 537-541
10. M.Z. Bian, T.T. Sasaki, B.C. Suh, T. Nakata, S. Kamado, K. Hono, A heat treatable Mg-Al-Ca-Mn-Zn sheet alloy with good room temperature formability, *Scripta Mater.* 138, 2017, 151-155
11. D. Guan, W.M. Rainforth, J. Gao, J. Sharp, B. Wynne, L. Ma, Individual effect of recrystallization nucleation sites on texture weakening in magnesium alloy: part 1- double twins, *Acta Mater* 135, 2007, 14-24
12. Y. Chino, X. Huang, K. Suzuki, K. Sassa, M. Mabuchi, Influence of Zn concentration on stretch formability at room temperature of Mg-Zn-Ce alloy, *Mater. Sci. Eng. A* 528, 2010, 566-572
13. Y. Chino, X. Huang, K. Suzuki, M. Mabuchi, Enhancement of stretch formability at room temperature by addition of Ca in Mg-Zn alloy, *Mater. Trans.* 51-4, 2010, 818-821
14. M. Yuasa, N. Miyazawa, M. Hayashi, M. Mabuchi, Y. Chino, Effects of group II elements on the cold stretch formability of Mg-Zn alloys, *Acta Mater.* 83, 2015, 294-303
15. N. Stanford, M.R. Barnett, The origin of "rare-earth" texture development in extruded Mg-based alloys and its effects on tensile ductility, *Mater. Sci. Eng. A* 496, 2008, 399-408
16. I. Basu, T. Al-Samman, G. Gottstein, Shear band-related recrystallization and grain growth in two rolled magnesium-rare earth alloys, *Mater. Sci. Eng. A*, 579, 2013, 50-56
17. Z.R. Zeng, Y.M. Zhu, S.W. Xu, M.Z. Bian, C.H.J. Davies, N. Birbilis, J. F. Nie, Texture evolution during static recrystallization of cold rolled magnesium alloys, *Acta Mater* 105, 2016, 479-494

18. E. Ball, P. Prangnell, Tensile-Compressive yield asymmetries in high strength wrought magnesium alloys, *Scripta Mater.* 31, 1994, 111-116
19. N. Standford, D. Atwell, A. Beer, C. Davies, M.R. Barnett, Effect of microalloying with rare earth elements on texture of extruded magnesium based alloys, *Scripta Mater.* 59, 2008, 772-775
20. J.P. Hadorn, K. Hantzsche, S. Yi, J. Bohlen, D. Letzig, S.R. Agnew, Effects of solute and second phase particles on the texture of Nd-containing Mg alloys, *Metall. Mater. Trans. A43*, 2012, 1363-1375
21. J.F. Nie, Y.M. Zhu, J.Z. Liu, X.Y. Fang, Periodic segregation of solute atoms in fully coherent twin boundaries, *Science* 340 (2013) 957-960
22. I. Basu, K.G. Pradeep, C. Mießen, L.A. Barrales-Mora, T. Al-Samman, The role of atomic segregation in designing highly ductile magnesium alloys, *Acta Mater.* 116, 2016, 77-94
23. K.Y. Zhu, D. Chaubet, B. Bacroix, F. Brisset, A study of recovery and primary recrystallization mechanisms in a Zr-2Hf alloy, *Acta Mater* 53, 2005, 5131-5140
24. R. Hielscher, H. Schaeben, A novel pole figure inversion method: specification of the MTEX algorithm, *J. Appl. Crystallogr.* 41, 2008, 1024-1037
25. D. Klaumünzer, J. Victoria-Hernandez, S. Yi, D. Letzig, S.H. Kim, J.J. Kim, M.H. Seo, K. Ahn, Magnesium process and alloy development for applications in the automotive Industry, *The Minerals, Metals and Materials Society, Magnesium Technology*, 2019, edited by V. Joshi et al, doi: 10.1007/978-3030-05789-3_3
26. J.S. Carpenter, T. Nizolek, R.J. McCabe, M. Knezevic, S.J. Zheng, B.P. Eftink, J.E. Scott, S.C. Vogel, T.M. Pollock, N.A. Mara, I.J. Beyerlein, Bulk texture evolution of

- nanolamellar Zr-Nb composites processed via accumulative roll bonding, *Acta Mater* 92, 2015, 97-108
27. K.Y. Zhu, B. Bacroix, T. Chauveau, D. Chaubet, O. Castelnau, Texture evolution and associated nucleation and growth mechanisms during annealing, *Metall Mater Trans A* 40, 2009, 2423-2434
28. X. Huang, K. Susuki, Y. Chino, Different annealing behaviours of warm rolled Mg-3Al-1Zn alloy sheets with dynamic recrystallized microstructure and deformation microstructure, *Mater. Sci. Eng. A* 560, 2013, 232-240
29. J. Victoria-Hernandez, S. Yi, J. Bohlen, G. Kurz, D. Letzig, The influence of the recrystallization mechanisms and grain growth on the texture of a hot rolled AZ31 during subsequent recrystallization annealing, *J. Alloys Compd.* 616, 2014, 189-197
30. F. Wagner, N. Bozzolo, O. Van Landuyt, T. Grosdidier, Evolution of recrystallization texture and microstructure in low alloyed titanium sheets, *Acta Mater.* 50, 2002, 1245-1259
31. S.I. Wright, M.M. Nowell, D.P. Field, A review of strain analysis using electron backscatter diffraction, *Microsc. Microanal.* 17 (2011) 316–329
32. D. Guan, W.M. Rainforth, L. Ma, B. Wynne, J. Gao, Twin recrystallization mechanisms and exceptional contribution to texture evolution during annealing in a magnesium alloy, *Acta Mater.* 126, 2017, 132-144
33. S. Nourbakhsh, T.D. O'Brien, Texture formation and transition in cold-rolled titanium, *Mater. Sci. Eng.* 100, 1988, 109-114
34. A. Gosh, A. Singh, N.P. Gurao, Effect of rolling mode and annealing temperature on microstructure and texture of commercially pure titanium, *Mater. Charact.* 125, 2017, 83-93

35. T.Sakai, A. Belyakov, R. Kaibyshev, H. Miura, J.J. Jonas, Dynamic and post-dynamic recrystallization under hot, cold and severe plastic deformation, *Prog. Mater. Sci.* 60, 2014, 130-207
36. I. Basu, T. Al-Samman, Twin recrystallization mechanisms in magnesium-rare earth alloys, *Acta Mater.* 96, 2015, 111-132
37. J. Victoria-Hernández, J. Suh, S. Yi, J. Bohlen, W. Volk, D. Letzig, Strain induced selective grain growth in AZ31 Mg alloy sheet deformed by equal channel angular pressing, *Mater. Charact.* 113, 2016, 98-107
38. S. Yi, I. Schestakow, S. Zaeferrer, Twinning-related microstructural evolution during hot rolling and subsequent annealing of pure magnesium, *Mater. Sci. Eng. A* 516, 2009, 58-64
39. T. Al-Samman, K. D. Molodov, D. Molodov, G. Gottstein, S. Suwas, Softening and dynamic recrystallization in magnesium single crystals during c-axis compression, *Acta Mater.* 60, 2012, 537-545
40. K.D. Molodov, T. Al-Samman, D.A. Molodov, G. Gottstein, Mechanisms of exceptional ductility of magnesium single crystal during deformation at room temperature: multiple twinning and dynamic recrystallization, *Acta Mater.* 76, 2014, 314-330
41. M. Jahedi, B.A. McWilliams, P. Moy, M. Knezevic, Deformation twinning in rolled WE43-T5 rare earth magnesium alloy: Influence on strain hardening and texture evolution, *Acta Mater* 131, 2017, 221-232
42. Y.B. Chun, C.H.J. Davies, The evolution of in-grain misorientation axes (IGMA) during deformation of wrought magnesium alloy AZ31, *Magnesium Tech. 2010, Proceedings of TMS Eds., S.R. Agnew, N.R. Neelameggham, E.A. Nyberg, and W.H. Sillekens, TMS, Seattle, WA, 2010, 433-437*

43. Y.B. Chun, M. Battaini, C.H.J Davies, S.K. Hwang, Distribution characteristics of in-grain misorientation axes in cold rolled commercially pure titanium and their correlation with active slip modes, *Metall. Mater. Trans. A*, 41, 2010, 3473-3487
44. J.P. Hadorn, K. Hantzsche, S. Yi, J. Bohlen, D. Letzig, J. Wollmershauser, S.R. Agnew, Role of solute in the texture modification during hot deformation of Mg-RE alloys, *Metall. Mater. Trans. A*, 43, 2012, 1347-1362
45. Z. Huang, L. Wang, B. Zhou, T. Fischer, S. Yi, X. Zeng, Observation of non-basal slip in Mg-Y by in-situ three-dimensional X-ray diffraction, *Scripta Mater.* 143, 2018, 44-48
46. L. Wang, Z. Huang, H. Wang, A. Maldar, S. Yi, J.S. Park, P. Kenesei, E. Lilleodden, X. Zeng, Study of slip activity in a Mg-Y alloy by in-situ high energy X-ray diffraction microscopy and elastic viscoplastic self-consistent modeling, *Acta Mater.* 155, 2018, 138-152
47. I. Basu, T. Al-Samman, Triggering rare earth texture modification in magnesium alloys by addition of zinc and zirconium, *Acta Mater.* 67, 2014, 116-133
48. M. Jahedi, B.A. McWilliams, M. Knezevic, Deformation and fracture mechanisms in WE43 magnesium-rare earth alloy fabricated by direct-chill casting and rolling, *Mater Scie Eng A* 726, 2018, 194-207
49. S. Ghorbanpour, B.A. McWilliams, M. Knezevic, Effect of hot working and aging heat treatments on monotonic, cyclic, and fatigue behavior of WE43 magnesium alloy, *Mater Scie Eng A* 747, 2019, 27-41
50. F.J. Humphreys, M. Hatherly, *Recrystallization and related annealing phenomena*, Elsevier, Oxford, 2004. P 211, 380

Figure captions:

Fig. 1 Microstructures of the a) as-TRC strip and b) after homogenization annealing at 450° for 16 h.

Fig. 2 Optical microstructures in a) as-rolled condition and b) after annealing at 370 °C for 1800 s.

Fig. 3 Microstructural development after annealing at 370 °C for a) 30 s, b) 90 s, c) 180 s and d) sample recrystallized at 370 °C for 1800 s and subsequently annealed at 450 °C for 1800 s.

Fig. 4 XRD textures represented in terms of (0001) and (10-10) pole figures for the a) as TRC strip and b) after homogenization annealing at 450 °C for 16 h.

Fig. 5 XRD textures represented in terms of (0001) and (10-10) pole figures for the a) as-rolled ZXK sheet and b) after recrystallization annealing at 370 °C for 1800 s.

Fig. 6 Texture evolution in terms of the (0001) pole figure for different annealing conditions. The intensity profiles are plotted as a function of the tilt from normal direction towards RD (90 and 270°) and TD (0-180°) for a) as-rolled state, b-e) annealed at 370 °C for 30, 90, 180, 1800 s respectively, and f) sample annealed at 370 °C for 1800 s plus an additional annealing at 450 °C for 1800 s.

Fig. 7 Texture representation in terms of ODF sections ($\varphi_2=0^\circ$ and $\varphi_2=30^\circ$) plotted with orthotropic symmetry for a) as-rolled sheet, b) annealed sample at 370 °C for 1800 s and c) ODF intensity plots for marked fibers denoted as "1" and "2" (see dotted lines in Fig. 7a) for the whole set of annealed samples.

Fig. 8 *Ex-situ* EBSD orientation image maps (OI) and related local texture in terms of the (0 0 0 1) and (1 0 -1 0) pole figures of a) hot rolled sample and after annealing at 350 °C for b) 270 s, c) 570 s and d) 1800 s.

Fig. 9 Discrete (0001) pole figure showing orientations corresponding to grains with *c*-axis deviating from ND to different ranges, i.e. $0^\circ < \text{ND deviation} \leq 30^\circ$, $30^\circ < \text{ND deviation} \leq 60^\circ$ and $60^\circ < \text{ND deviation} \leq 90^\circ$, towards RD and TD, respectively. a) As-rolled sample and b) sample annealed at 350 °C for 1800 s.

Fig. 10 True stress-true strain curves of s) as-rolled, b-d) samples annealed at 370 °C for 30, 90 and 1800 s, respectively.

Fig. 11 *Ex-situ* EBSD OI maps, fractions of the deformed ($\text{GOS} > 0.5^\circ$) and recrystallized ($\text{GOS} < 0.5^\circ$) fractions of the microstructure with corresponding KAM maps of a) as-rolled sample, b) sample annealed 270 s, c) sample annealed 570 s, and d) sample annealed 1800 s at 350 °C. In black: high angle grain boundaries ($\theta > 15^\circ$) and in white: low angle grain boundaries ($2^\circ < \theta < 14^\circ$).

Fig. 12 Discrete (0001) pole figure showing the orientation of 10 selected grains depicted in Fig. 11.

Fig. 13 *Ex-situ* image quality (IQ) maps from magnified images from areas marked in Fig. 8 for a) as-rolled sample, b) sample annealed 270 s and c) sample annealed at 350 °C for 570 s, and d) corresponding (0 0 0 1) and {1 1 -2 0} pole figures showing orientations of a deformed grain and related twin volume. In black: high angle grain boundaries ($\theta > 15^\circ$), in red: {1 0 -1 2} extension twins, in yellow: {1 0 -1 1} contraction twins and in green: {1 0 -1 1}-{1 0 -1 2} double

twins. (For interpretation of the references to colour in this figure legend, the reader is referred to the web version of this article).

Fig. 14 a) OI maps and respective discrete (0 0 0 1) pole figure showing the whole set of orientations, b-e) OI maps, respective discrete pole figure and IGMA distribution plots for different sets of grains divided according to their orientation.

Supplementary figures

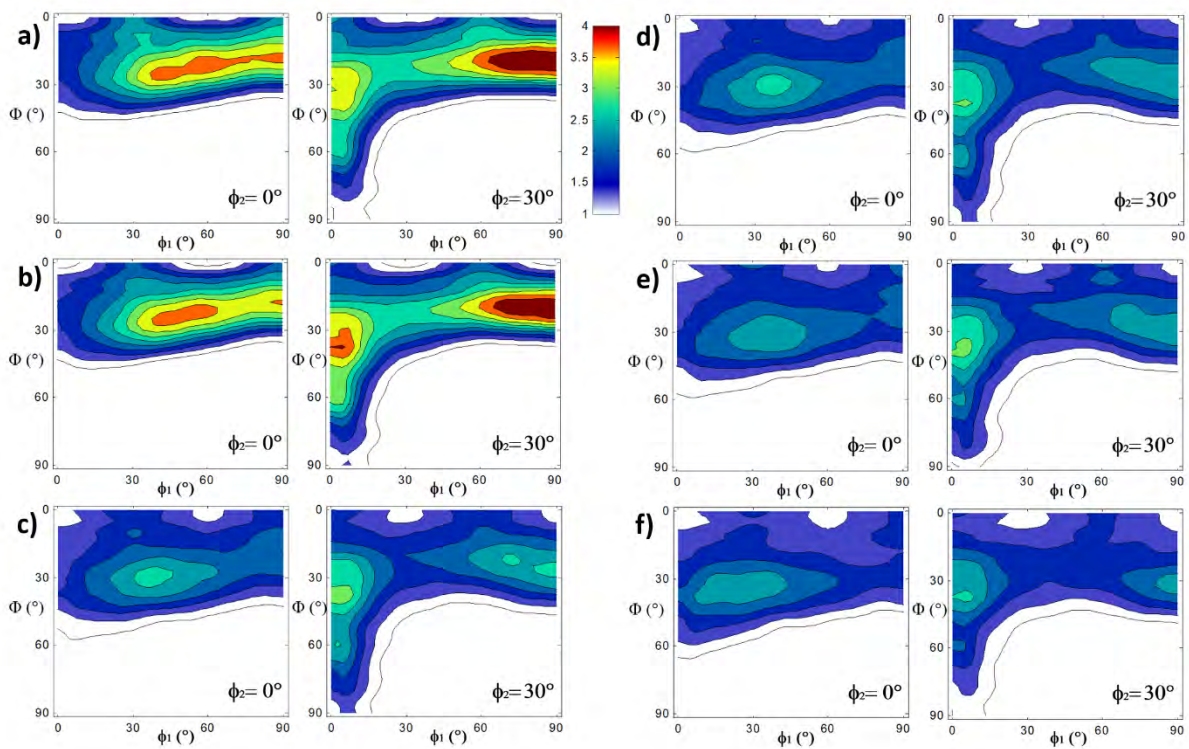


Fig. S1 Texture representation in terms of ODF sections ($\varphi_2=0^\circ$ and $\varphi_2=30^\circ$) for a) as-rolled sheet, b-e) samples annealed at 370 °C for 30 s, 90 s, 180 s and 1800 s, respectively; and f) sample annealed at 370 °C for 1800 s and subsequently annealed at 450 °C for 1800 s.

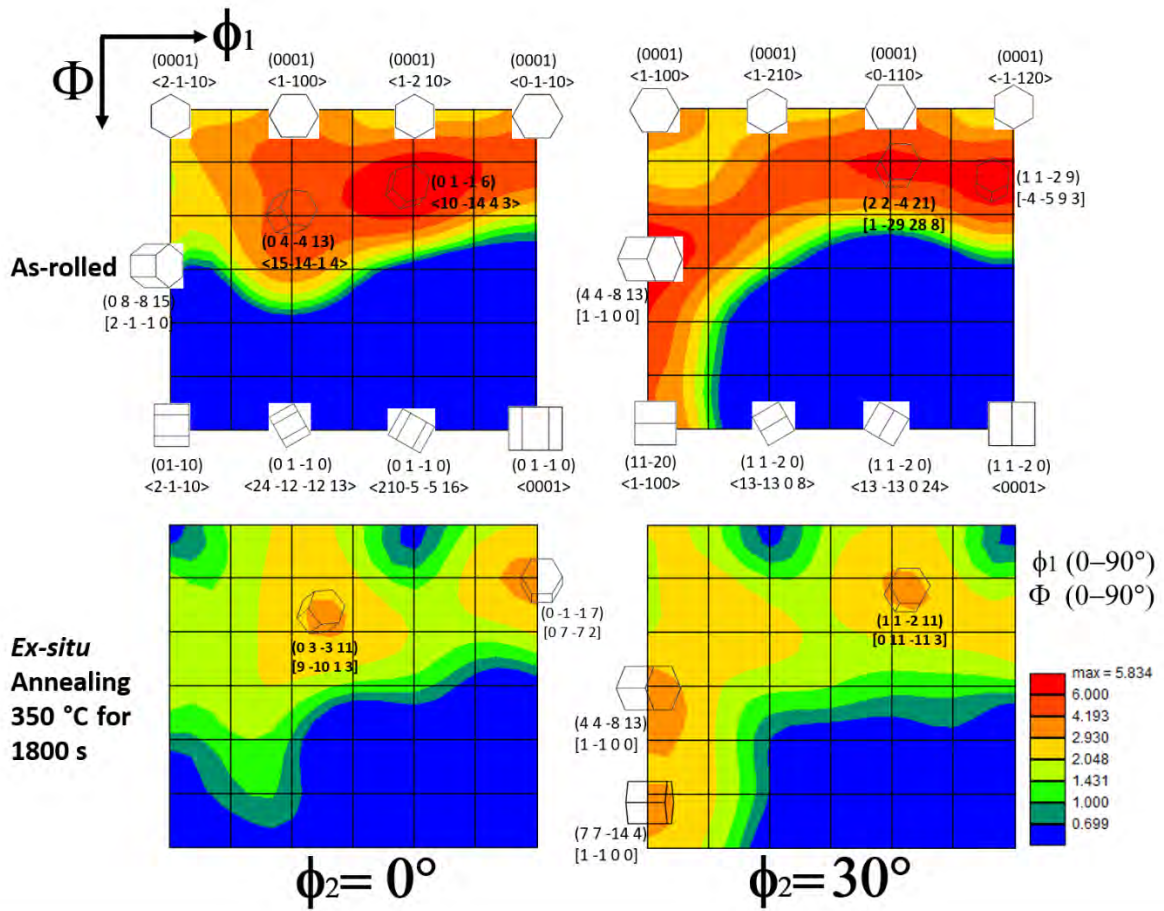
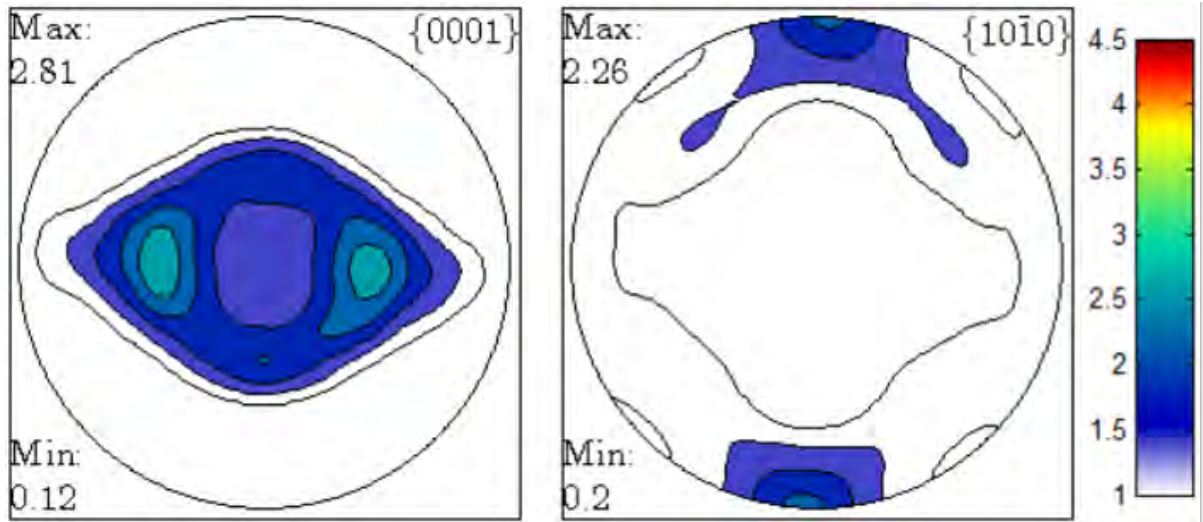


Fig. S2 Texture representation in terms of ODF sections ($\phi_2=0^\circ$ and $\phi_2=30^\circ$) calculated from EBSD data for a) as-rolled sheet and b) sample *ex-situ* annealed at 350 °C for 1800 s.



S3. (0 0 0 1) and (1 0 -1 0) poles of a sample annealed at 370 °C for 1800 s and subsequently annealed at 450 °C for 1800 s.